J. Fluid Mech. (2025), *vol.* 1021, A25, doi:10.1017/jfm.2025.10707

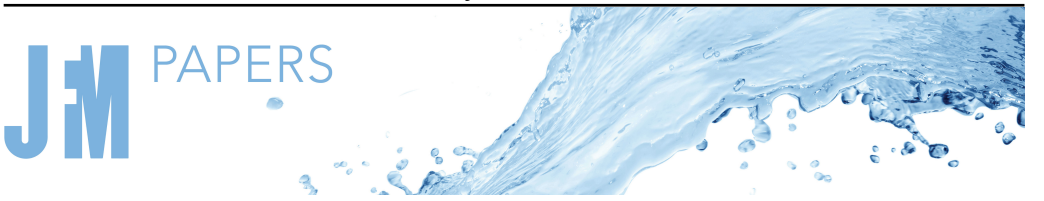

The spatio-temporal evolution of superstructures over rough-wall turbulent boundary layers

Ioannis K. Kaminaris[1], **Elias Balaras**[1] **and Michael Paul Schultz**[2]

[1]Department of Mechanical and Aerospace Engineering, The George Washington University, Washington, DC 20052, USA

[2]Department of Naval Architecture and Ocean Engineering, United States Naval Academy, Annapolis, MD 21402, USA

Corresponding author: Ioannis K. Kaminaris; Email: kaminaris@email.gwu.edu

(Received 1 May 2025; revised 4 August 2025; accepted 5 September 2025)

The spatio-temporal evolution of very large-scale coherent structures, also known as superstructures, is investigated in both smooth- and rough-wall boundary layers by means of direct numerical simulations up to a frictional Reynolds number of $Re_\tau = 3\,150$. One smooth-wall and four rough-wall cases are considered, all developing over a region as long as ∼60 times the incoming boundary-layer thickness in the streamwise direction. Bio-inspired, biofouling-type topographies are employed for the rough-wall cases, following the previous work of Womack *et al.* (2022 *J. Fluid Mech.* vol. 933, p. A38) and Kaminaris *et al.* (2023 *J. Fluid Mech.* vol. 961, p. A23). We utilise three-dimensional time series, as well as multiple two-point correlation functions along the boundary layer to capture the detailed length- and time-scale evolution of the superstructures. The results suggest that the presence of roughness significantly amplifies both the strength and the streamwise growth rate of superstructures. Interestingly, however, their ratios relative to the local boundary-layer thickness, $\mathscr{L}_x/\delta$ and $\mathscr{L}_z/\delta$, remain constant and independent of the streamwise coordinate, indicating that such scaled length scales might constitute a possible flow invariant. Volumetric correlations revealed that all cases induce structures inclined with respect to the mean-flow direction, with those over the rough-wall topographies exhibiting steeper inclination angles. Finally, via proper orthogonal decomposition, pairs of counter-rotating roll modes were detected and found to flank the high- and low-speed superstructures, supporting the conjecture in the literature regarding the mechanisms responsible for the lateral momentum redistribution. The latter also suggests that the way momentum organises itself in high Reynolds number wall-bounded flows might be independent of the roughness terrain underneath.

Key words: boundary layer structure, turbulent boundary layers, turbulence simulation

1. Introduction

The existence of coherent regions in the fluctuating velocity field near the wall, also known as streaks, is widely studied and demonstrated by numerous studies. These structures are known to exhibit widths of $\lambda^+ \approx 100$ and to maximise their spatial footprint at approximately the buffer layer ($5 \leqslant y^+ \leqslant 30$), beyond which they cease to exist (see for example Smith & Metzler 1983). The latter perception of the near-wall turbulence structure, however, was dramatically altered by the observations made in Kim & Adrian (1999), who reported evidence of very large coherent motions residing at wall-normal locations even greater than the logarithmic layer and extending up to 14 pipe diameters in length, based on dimensionless wavelengths of the streamwise velocity spectra. It was also conjectured by the authors that such structures incarnate the line up of low momentum regions induced by hairpin packets. The existence of such very large-scale motions over smooth-wall turbulent boundary layers was first reported in the experimental work of Hutchins & Marusic (2007), where they detected structures in instantaneous snapshots of up to 20δ in length, where δ the local boundary layer thickness. They termed them superstructures and observed that they exhibit a meandering behaviour, as well as a near-wall footprint. They also indicted that these structures are inclined in the streamwise direction and that they become the longest at the logarithmic region. Throughout the span of the last two decades various other studies reported estimations of the superstructures' length scales over smooth-wall boundary layers: Lee & Sung (2011) for example, identified length scales up to 6δ in their direct numerical simulations (DNS) at low/moderate Reynolds numbers, while Dennis & Nickels (2011) reported similar length scales up to 5δ by conditionally averaging the measured three-dimensional velocity field. Both studies have also associated superstructures with coexisting hairpin-style packets. Sillero, Jiménez & Moser (2014) on the other hand, by utilising two-point correlations of their DNS boundary-layer flow up to a momentum Reynolds number of $Re_\theta = 6680$, that were previously characterised via one-point statistics in Sillero, Jiménez & Moser (2013), reported streamwise lengths of the order of $\mathcal{O}(18\delta)$ and $\mathcal{O}(7\delta)$ for channel and boundary-layer configurations, respectively.

The near-wall impact of these structures was investigated by Marusic, Mathis & Hutchins (2010), who proposed a simple mathematical model that predicts the fluctuating near-wall velocity signal based on large-scale information from the logarithmic region of the boundary layer. They also conjectured the existence of counter-rotating streamwise coherent vortices that are encharged with the momentum redistribution between the high- and low-speed superstructures. Direct numerical simulations were also used by Lee, Sung & Zaki (2017) to analyse the effect of large-scale structures on the turbulent/non-turbulent interface of smooth-wall turbulent boundary layers, by employing a vorticity-based threshold which allowed for the separation of the fluid motions inside and outside the boundary layer. The importance of the large-scale structures to the near-wall turbulence was investigated by Örlü & Schlatter (2011), where, surprisingly, it was found that the energy spectra of the fluctuating wall-shear stress in inner coordinates exhibited significant deviation at large wavelengths over a range of different Re, highlighting the influence of outer-layer structures at the wall. The latter were also investigated by Marusic *et al.* (2021), where it was reported that the contribution of large-scale motions of the outer layer to the variance of the fluctuating wall-shear stress was significant, ranging from 8 % to 30 % for $Re_\tau = 10^3$ and $Re_\tau = 10^5$, respectively. The meandering behaviour of the smooth-wall superstructures is discussed in detail in Kevin *et al.* (2019*a*), where it was concluded that superstructures tend to meander more as the wall-normal distance increases. Deshpande *et al.* (2023), by computing two-point correlations of the wall-normal velocity fluctuations in turbulent boundary layers up to $Re_\tau \approx 7500$, provided support that wall-normal-scaled geometrically self-similar motions might be the constituents forming the superstructures.

On the other hand, the existence of a rough wall is known to significantly impact the mean-flow structure and specifically the outer-layer similarity with parameters such as the roughness Reynolds number, k_s^+, and the blockage ratio, δ/k (k a characteristic roughness height), playing crucial roles (see for example Jiménez 2004; Chung *et al.* 2021; Squire *et al.* 2016*b*). Thus, the question regarding how much roughness impacts the spatio-temporal evolution of these structures remains largely unexplored, but there is evidence that there is a significant change in the overall dynamics. For example, Volino, Schultz & Flack (2007) made extensive comparisons between the flow structure in a smooth- and a rough-wall (of woven mesh type) surface using two-point correlations and concluded that the flow length scales in the case of the latter were found to be reduced compared with the smooth-wall surface. They reported, however, that an excellent qualitative agreement was obtained in regard to the outer part of the boundary layer between the two surfaces, providing further support to the existence of the outer-layer similarity hypothesis (see Townsend 1976). Extensive smooth- and rough-wall comparisons of two-point correlation statistics were also made in Wu & Christensen (2010), where rough-wall structures were also found to result in shorter correlation lengths, in agreement with Volino *et al.* (2007). Similar observations were also made in Squire *et al.* (2016*a*) with the exception of some deviation at reference heights with greater wall-normal locations in the case of their particle image velocimetry (PIV) measurements. Lee, Kim & Lee (2016) investigated the effects of canonical roughness on the streamwise velocity fluctuating structures using DNS in a spatially developing turbulent boundary-layer set-up of relatively low Re ($Re_\theta = 930$–1 800) over regularly arranged two-dimensional (2-D) rod roughness. They observed an increase in the characteristic correlation length scale in the presence of rods, when compared with the smooth-wall ones. Similarly, Kevin *et al.* (2019*b*) investigated the superstructures' behaviour in the case of converging–diverging riblet surfaces and estimated their lengths at approximately $4-5\delta$. Furthermore, the extent of the superstructure streamwise coherence in the case of a topography with spanwise alternating smooth and rough strips has been also examined in Wangsawijaya *et al.* (2020) and Wangsawijaya & Hutchins (2022), and it was estimated to be of the order of 3–4 boundary-layer thicknesses.

In spite of the extensive literature regarding the length scale of the superstructures, most of the studies are confined to measurements performed over a single streamwise location of the boundary layer. Furthermore, common experimental limitations, such as the streamwise extent of the PIV windows, which is in the order of $1.5-10\delta$ result in the interruption of the streamwise superstructure coherence which at some instances can reach up to 20δ. On the other hand, numerical works that can capture complete structures are restricted to low Re_τ, at which the existence of superstructures is somehow subtle. So far, no study has attempted to capture their spatio-temporal evolution along rough-wall turbulent boundary layers at higher Reynolds numbers, and outside the canonical roughness regime discussed above very little is known regarding the behaviour of superstructures over complex multi-scale rough-wall topographies. In the present work, we report DNS of turbulent boundary layers with zero pressure gradients developing over both smooth and rough walls, which comprise bio-inspired topographies. Specifically, biofouling-type surfaces are employed that mimic common marine organisms in one staggered and three random arrangements. From this database we extract information regarding superstructure growth within the boundary layer over various surfaces, as well as regarding the cross-stream momentum re-organisation by performing a modal analysis. Below, the details of the DNS set-up are reported in § 2. Next, the spatio-temporal evolution of the superstructures over both smooth and rough walls is discussed in § 3, while the lateral momentum redistribution in the instantaneous field is investigated by means of proper orthogonal decomposition (POD) in § 4.

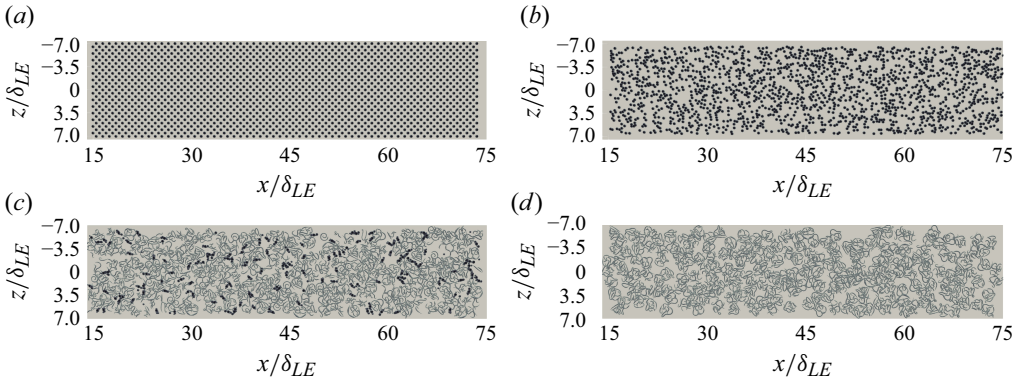

Figure 1. Top view of the biofouling-type topographies. Panels show (*a*) BS39; (*b*) BR39; (*c*) MR39; (*d*) TR39.

Topography	Planar solidity	Frontal solidity	Mean roughness height	Mean organism height	Standard deviation	Skewness	Kurtosis	Effective Slope	Roughness Reynolds number	Symbols
	λ_p (%)	λ_f (%)	$\overline{h}/\delta_{LE}$	$\hbar/\delta_{LE}$	σ/δ_{LE}	Sk	Ku	ES_{xz}	k_s^+	
Smooth	—	—	—	—	—	—	—	—	—	▲
BS39	39.3	15.9	0.0460	0.090	0.0740	1.409	3.520	0.317	570	◆
BR39	39.2	15.5	0.0488	0.097	0.0768	1.311	3.200	0.310	470	■
MR39	40.2	14.73	0.0266	0.0617	0.0430	1.872	6.826	0.279	175	●
TR39	40.1	13.11	0.0209	0.0474	0.0310	1.173	2.826	0.248	105	▼

Table 1. Surface characteristics for the biofouling-type topographies considered in this work.

2. Computational set-up

The current work employs bio-inspired surfaces of biofouling type that are commonly found on the hulls of naval vessels (see for example Schultz 2007). Specifically, four topographies are considered, one in a staggered arrangement (BS39) comprising only barnacle-type organisms and three in random arrangements comprising (i) only barnacle-type (BR39) organisms, (ii) only tubeworm-type (TR39) organisms and (iii) a mixture (MR39) of barnacle- (20 %) and tubeworm-type (80 %) organisms (see figure 1). The barnacle-type organisms are modelled via truncated cones, following the work of Womack *et al.* (2022), while the tubeworm-type organisms are designed to mimic scans of actual organisms found on ship hulls (see Kaminaris & Balaras 2024, for details). All topographies have the same surface coverage, $\lambda_p \approx 40$ %, and frontal solidity, $13.11\ \% < \lambda_f < 15.9\ \%$ while they all have skewness, $Sk > 1$, which is characteristic of biofouling surfaces. The main difference between the barnacle-type (BS39, BR39) and the mixed-(MR39) or tubeworm-type (TR39) topographies is the mean height, which is $\overline{h}/\delta_{LE} \approx 0.045$ for the former and $\overline{h}/\delta_{LE} \approx 0.025$ for the latter (δ_{LE} is the boundary-layer thickness at the leading edge of the roughness). The key surface statistics for all topographies are listed in table 1. Furthermore, all flows are fully rough, $k_s^+ > 100$. A smooth-wall flat plate is also analysed as a reference case.

The computational domain is shown in figure 2(*b*), where the roughness patch is positioned $15\delta_{LE}$ downstream from the inflow plane and extends $60\delta_{LE}$, followed by

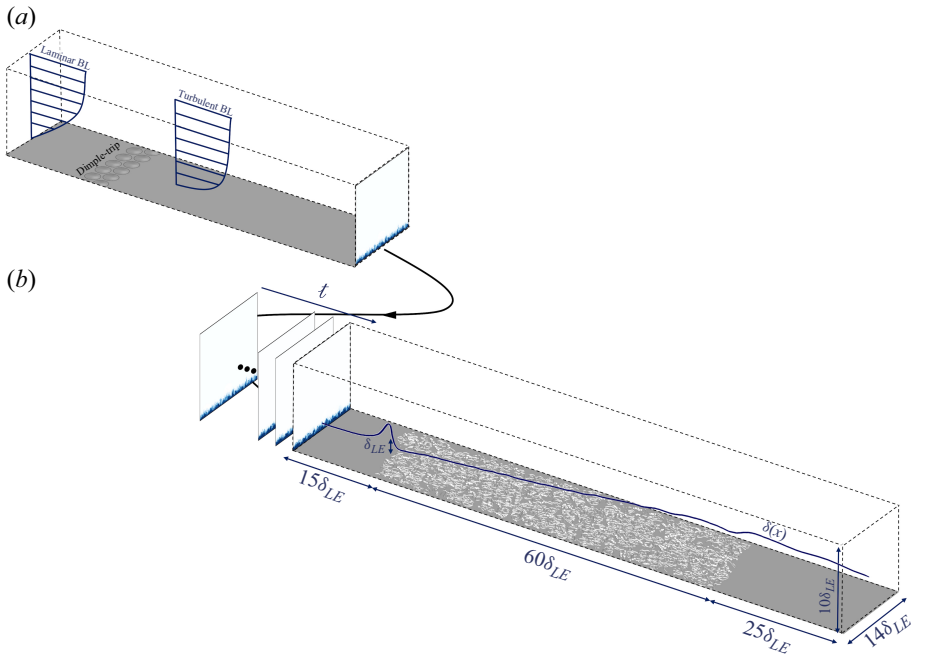

Figure 2. Schematic of the computational domain. (*a*) Precursor simulation; (*b*) production runs.

another smooth-wall portion. The overall dimensions of the computational domain are $100\delta_{LE} \times 14\delta_{LE} \times 10\delta_{LE}$ in the streamwise, spanwise and wall-normal directions, respectively. A precursor simulation is performed to extract velocity boundary conditions for the inflow plane: a laminar boundary layer is tripped by a dimple topography and is sampled at the streamwise distance where the desired Reynolds number is matched (see figure 2*a*). A structured Cartesian grid is used, and the boundary conditions on the roughness surface are imposed via an immersed boundary method (Balaras 2004). The grid within the roughness area is approximately uniform in all directions placing $40 \times 40 \times 70$ points in the streamwise, spanwise and wall-normal directions, respectively, for each barnacle organism. For the case of tubeworm organisms, their maximum dimension is resolved with approximately 140 grid points. This translates into a grid resolution of $\Delta x^+ = 10.5$, $\Delta z^+ = 9$ and $0.9 \leqslant \Delta y^+ \leqslant 20$ (based on the friction velocity, u_τ, on the smooth part of the plate), while the resolution in terms of Kolmogorov units is $\Delta y/\eta \sim 1.9$ right above the roughness crest of the barnacle-type surfaces, which is the location where η becomes the smallest, and everywhere in the domain less than 6. For details on the grid resolution, the boundary conditions, as well as the numerical methods employed in the current study see Kaminaris *et al.* (2023). In the latter, a detailed validation against the experimental work of Womack *et al.* (2022) is also provided. It is noted that the friction Reynolds number range obtained between the leading edge and trailing edge of the roughness patch for the rough-wall topographies is $1700 \leqslant Re_{\tau,rough} \leqslant 3150$, and $750 \leqslant Re_{\tau,smooth} \leqslant 1300$ for the smooth-wall case.

3. Superstructure evolution

First, in order to establish the impact each rough-wall case has on the mean flow, the boundary-layer evolution is presented in figure 3(*a*), by means of the boundary-layer thickness, δ/δ_{LE} over all the topographical cases studied herein. It can be clearly

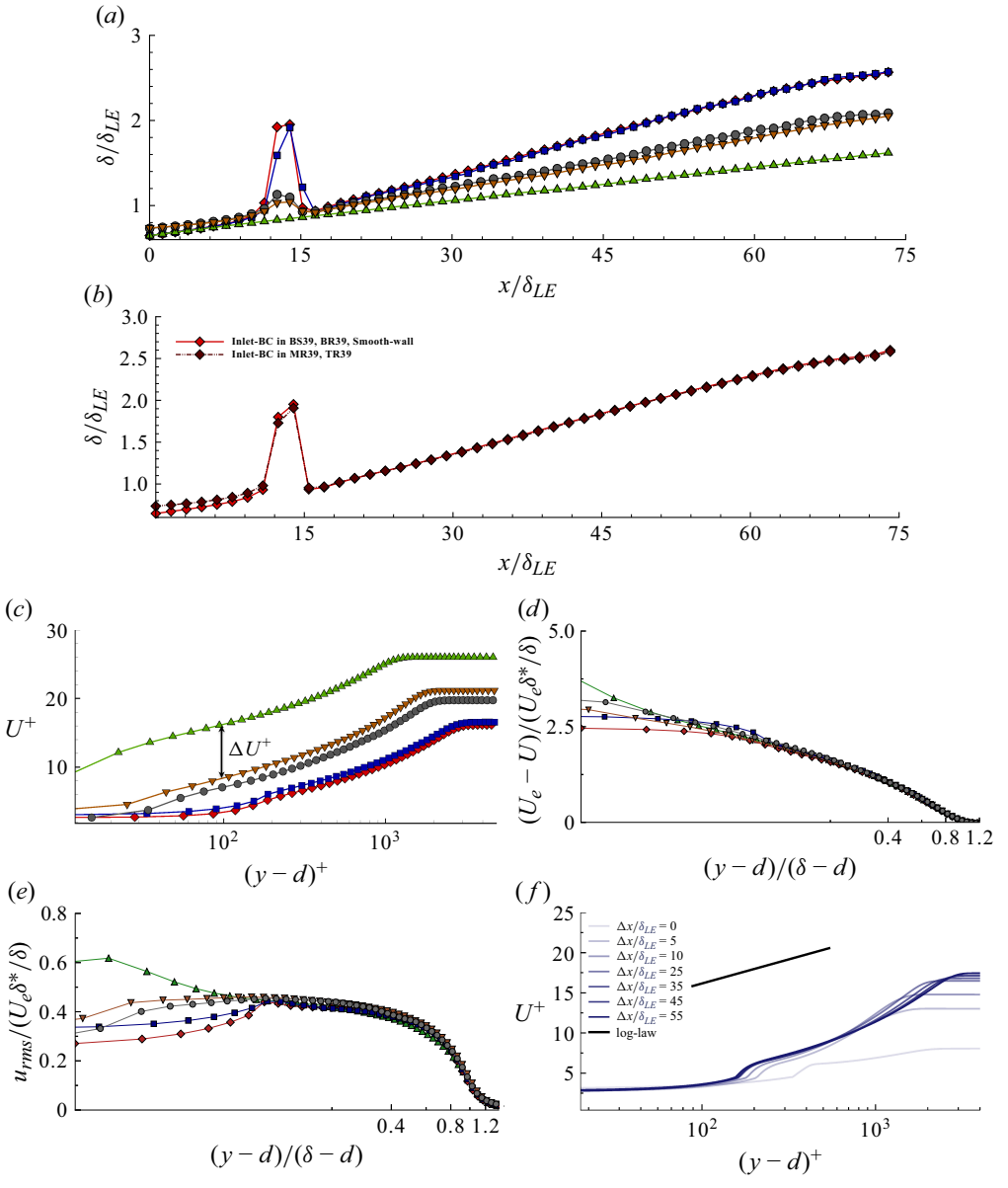

Figure 3. (*a*) Streamwise evolution of the boundary-layer thickness, δ/δ_{LE}; (*b*) comparison of the streamwise evolution of the boundary-layer thickness, δ/δ_{LE} in the case of the BS39 case between the two different inlet boundary conditions used (see legend for details); (*c*) mean streamwise velocity profiles in inner coordinates at $x/\delta_{LE}=65$; (*d*) mean streamwise velocity profiles in defect law at $Re_\tau\approx 2100$; (*e*) streamwise velocity root-mean-square profiles in outer coordinates at $Re_\tau\approx 2100$; (*f*) streamwise velocity profiles in inner coordinates separated by a streamwise distance. For clarity symbols in (*a*)–(*b*) correspond to every hundredth streamwise point, while (*c*)–(*e*) correspond to every fifth wall-normal point. ▲ Smooth wall; ◆ BS39; ■ BR39; ● MR39; ▼ TR39.

seen that the presence of roughness significantly impacts the boundary-layer growth, while the topographies with higher mean roughness heights, $\overline{h}$ (corresponding to higher barnacle-type concentrations) exhibit the highest growth rate. The surface cases BS39 and BR39, which all comprise approximately same height roughness elements, show minimal

differences despite their different distributions. The hump formed in the boundary-layer thickness at the leading edge of the roughness is the result of the significant blockage ratios, $\overline{h}/\delta_{LE}$, which imposes pressure drag by the roughness and redirects the flow to overcome the roughness elements. It is noted that there is a small difference of $\approx$7 % in the Reynolds number at the inlet of the computational domain between the smooth, BS39, BR39 and the MR39, TR39 cases, which, however, was not found to result in any difference in the boundary-layer evolution over the rough-wall patch according to a numerical experiment performed in the BS39 case (please see figure 3*b*). Therefore, the inlet boundary condition is treated as same for all cases. To further quantify the roughness impact on the mean flow the streamwise velocity profile in inner coordinates is provided in figure 3(*c*). Through the latter, it can be seen that the roughness function, ΔU^+, which encapsulates the momentum deficit due to the presence of the roughness, also increases as the mean roughness height increases, similarly to the observations made regarding the boundary-layer growth. On the other hand, despite the significant impact the roughness has in the near-wall region, the outer part of the flow seems to behave similarly and independent of the topographical terrain underneath, as suggested by the mean streamwise velocity and streamwise velocity root-mean-square profiles in figure 3(*d*,*e*), plotted using the velocity scale introduced by Zagarola & Smits (1998) and further validated in boundary-layer configurations by Connelly, Schultz & Flack (2006). It is noted that the small differences between the rough- and smooth-wall data in figure 3(*e*) are expected and due to the difference in Re_τ between the cases, given that the maximum smooth-wall friction Reynolds number is $Re_\tau \approx 1\,300$ while the rough-wall $Re_\tau \approx 2\,100$ ($Re_\tau = u_\tau \delta/\nu$, where u_τ and δ is the local friction velocity and boundary-layer thickness), while ν is the kinematic viscosity. Note that the local friction velocity is computed via direct force integration on the surface (see Kaminaris *et al.* 2023 for details). The strong dependency of the Reynolds stresses on the Reynolds number is highlighted in great detail in Squire *et al.* (2016*b*) and Sillero *et al.* (2013). Finally, the equilibrium state of the boundary layer is demonstrated via figure 3(*f*), where multiple streamwise velocity profiles are plotted along the boundary-layer evolution. The latter should not be taken for granted, since the boundary-layer flows of the present work initially develop over a smooth-wall region before entering the rough-wall patch and thus they carry some transition effects. Immediately downstream of the leading edge of the roughness the boundary layers have not yet reached an equilibrium state, which is eventually achieved after some development region. Figure 3(*f*) indicates that the flow herein starts following the canonical velocity profile again at $\approx 10\delta_{LE}$ downstream of the leading edge of the roughness. The latter was also found to be largely the same for all the surfaces considered. Note the symbol d used in figure 3(*c*–*f*) corresponds to the zero-plane displacement, namely the virtual wall origin, that is, the distance which the wall has to be shifted to yield the same slope of the rough-wall logarithmic layer as the smooth-wall one, given the same constants κ and B.

Figure 4 presents a top view of iso-surfaces of positive and negative instantaneous streamwise velocity fluctuations, $u'(\underline{x}, t) = u(\underline{x}, t) - \overline{u}(\underline{x})$ (where $\underline{x} = x\hat{i} + y\hat{j} + z\hat{k}$), highlighting the superstructures. Qualitatively, the superstructures become stronger and wider as they grow within the rough-wall patches compared with the smooth-wall ones, despite the fact that, in all simulations, the same boundary layer enters the domain of interest. Furthermore, the known tendency of the smooth-wall superstructures towards streamwise misalignment (also known as meandering) is also observed in the rough-wall topographies. In regard to the superstructures formed over the topographies with lower mean heights, $\overline{h}$, (i.e. topographies with lower barnacle-type concentrations) shown in figure 4(*d*,*e*), it can be seen that they form a more slender shape compared with the increased mean heights ones (i.e. increased barnacle-type concentrations) of figure 4(*b*,*c*).

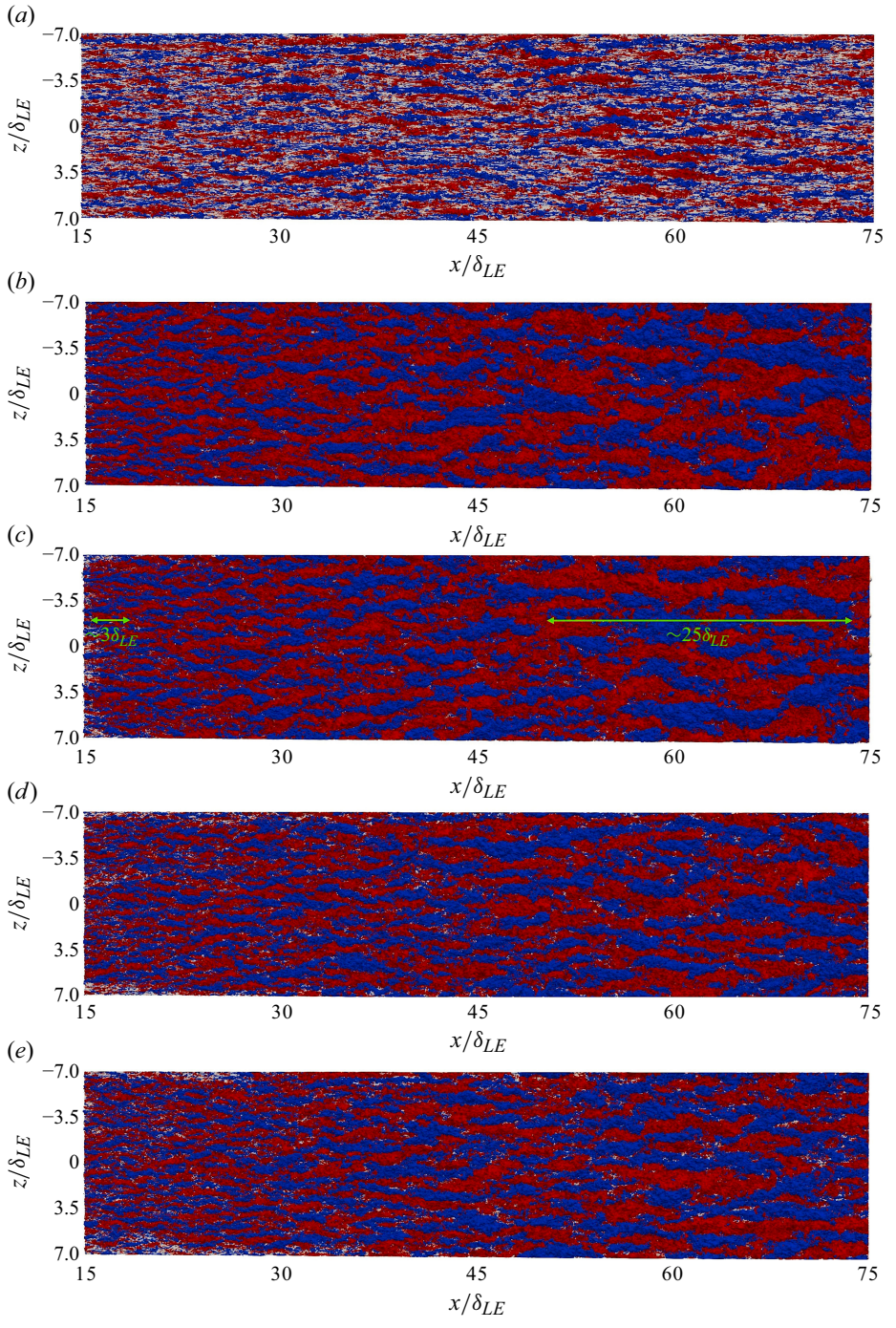

Figure 4. Top view of the isosurfaces of the streamwise velocity fluctuations, u', in the cases of (*a*) smooth wall; (*b*) BS39; (*c*) BR39; (*d*) MR39; (*e*) TR39. Positive isosurface $u'/U_e = 0.13$ shown in red and negative isosurface $u'/U_e = -0.13$ shown in blue. Green lines indicate the lengths of two typical structures at the upstream and downstream part of the BR39 topography.

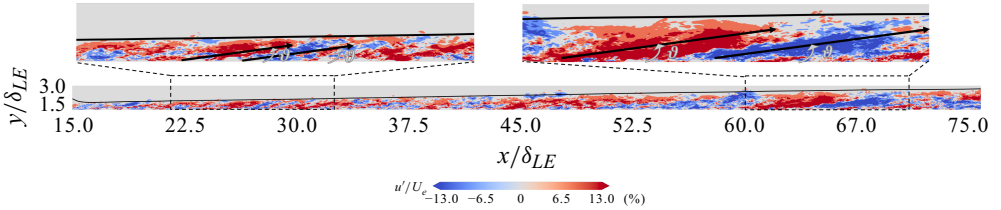

Figure 5. Side view of the contours of streamwise velocity fluctuations, u'/U_e, in the case of the rough wall with the random BR39 case.

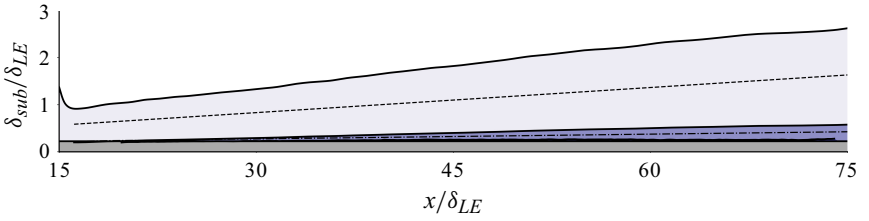

Figure 6. Streamwise evolution of the boundary-layer sublayers for BR39 case. Outer layer represented by lighter blue colour and its centreline by − − −; Logarithmic layer represented by darker blue colour and its centreline by —·—.

The significant growth the superstructures exhibit is highlighted in figure 4(*c*), where both an upstream small superstructure of approximately $3\delta_{LE}$ length and a downstream one of approximately $25\delta_{LE}$ are indicated. In line with previous works (see for example Kevin *et al.* 2019*a*, 2019*b*) we see that, also for the case of rough walls, these structures exhibit a streamwise inclination, which results in superstructures climbing to neighbouring ones of opposite sign as they evolve downstream (figure 5). This inclination is present throughout the boundary-layer evolution and qualitatively at almost constant angles of around 8°.

In order to estimate the superstructure length, the time- and spanwise-averaged two-point correlations of the streamwise velocity fluctuations with respect to the streamwise lag are computed as

$$R^{x}_{u'u'}(x,\, y,\, \Delta x) = \left\langle \sum_{n=1}^{N_x} \left[u'(x,\, y,\, z,\, t) u'(x+\Delta x,\, y,\, z,\, t)\right] / \sum_{n=1}^{N_x} \left[u'^2(x,\, y,\, z,\, t)\right] \right\rangle_{z,t}, \tag{3.1}$$

and presented in figure 7 for three different wall-normal locations: (i) the viscous sublayer/roughness sublayer (here referring to the wall-normal distance between the roughness crest an the onset of the logarithmic layer), (ii) the logarithmic layer and the (iii) outer layer. The two-point correlation functions are widely accepted as a rigorous way of estimating a signal correlation length and here are computed in a window of 10δ-length, centred at $x/\delta_{LE} = 62.5$. It should be noted that, despite the superstructure extent across the whole boundary-layer height, as was shown in figure 5, it is of interest to investigate their length-scale dependency on the wall-normal distance relative to the location of the three major sublayers. Thus, the normalised two-point correlations are computed at the centreline of each sublayer, which is tracked in space following the boundary-layer growth, as shown in figure 6. The sublayer limits are estimated based on the inner-scaled streamwise velocity profile (see figure 3*c*). Specifically, the start of the outer layer is considered at $y/\delta = 0.145$ for the smooth wall, at $y/\delta = 0.19$ for the BS39, at $y/\delta = 0.195$ for the BR39, at $y/\delta = 0.148$ for the MR39 and at $y/\delta = 0.14$ for the TR39 topography. In the context of the current paper, the roughness sublayer refers to

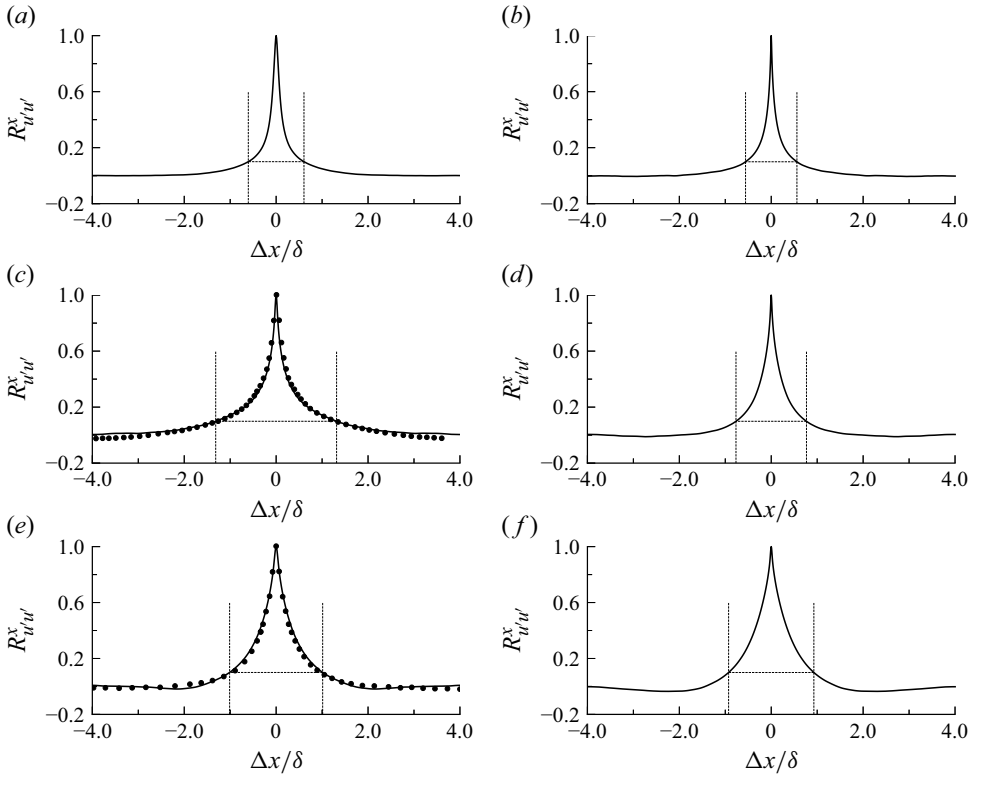

Figure 7. Streamwise two-point correlations of the streamwise velocity fluctuations, $R^x_{u'u'}$, at $x/\delta_{LE} = 62.5$ and various wall-normal locations. Left side: smooth wall, $Re_\tau = 1150$; right side: BR39 case, $Re_\tau = 2900$; (*a*,*b*) at the centreline of viscous/roughness sublayer ($y/\delta_{smooth} = 0.005$, $y/\delta_{BR39} = 0.097$); (*c*,*d*) at the centreline of the logarithmic layer ($y/\delta_{smooth} = 0.083$, $y/\delta_{BR39} = 0.15$); (*e*,*f*) at the centreline of the outer layer ($y/\delta_{smooth} = 0.57$, $y/\delta_{BR39} = 0.59$); • experiments by Hutchins & Marusic (2007) at $Re_\tau = 1120$; dashed lines correspond to the correlation cutoff of $R^x_{u'u'} = 0.1$.

the thin layer immediately above the roughness peak and the start of the logarithmic layer, as defined by the mean streamwise velocity profile in inner coordinates. The correlation length, $\mathscr{L}_x$, is defined as the distance between the first two symmetric crossings of the $R^x_{u'u'}$ distribution at the 0.1 cutoff ordinate. By looking at figure 7(*a*,*c*,*e*) one can see that the streamwise extent of the smooth-wall superstructures increases as one moves away from the wall and becomes maximum in the logarithmic layer, beyond which it decreases again. The latter also verifies the observations made in Hutchins & Marusic (2007), whose two-point correlations are superposed in figure 7(*c*,*e*) and shown in black circles, indicating an excellent agreement between the two studies. On the other hand, the streamwise extent of the superstructures, in the case of the BR39 arrangement, grows linearly with the wall-normal distance, as shown in figure 7(*b*,*d*,*f*). The same trends were obtained for the rest of the rough-wall cases, which are not shown here for the sake of brevity. Interestingly, the streamwise extent of the superstructures in the case of the rough walls is found to be reduced compared with the corresponding one of the smooth wall. However, it is noted that, in the present figures, the correlation lags are scaled by the local boundary-layer thickness, δ, extracted from the middle of the correlation window, which in the case of the rough walls is significantly increased. The rough-wall boundary-layer evolution is not universal, but rather dependent on each specific topography studied, and as will be shown

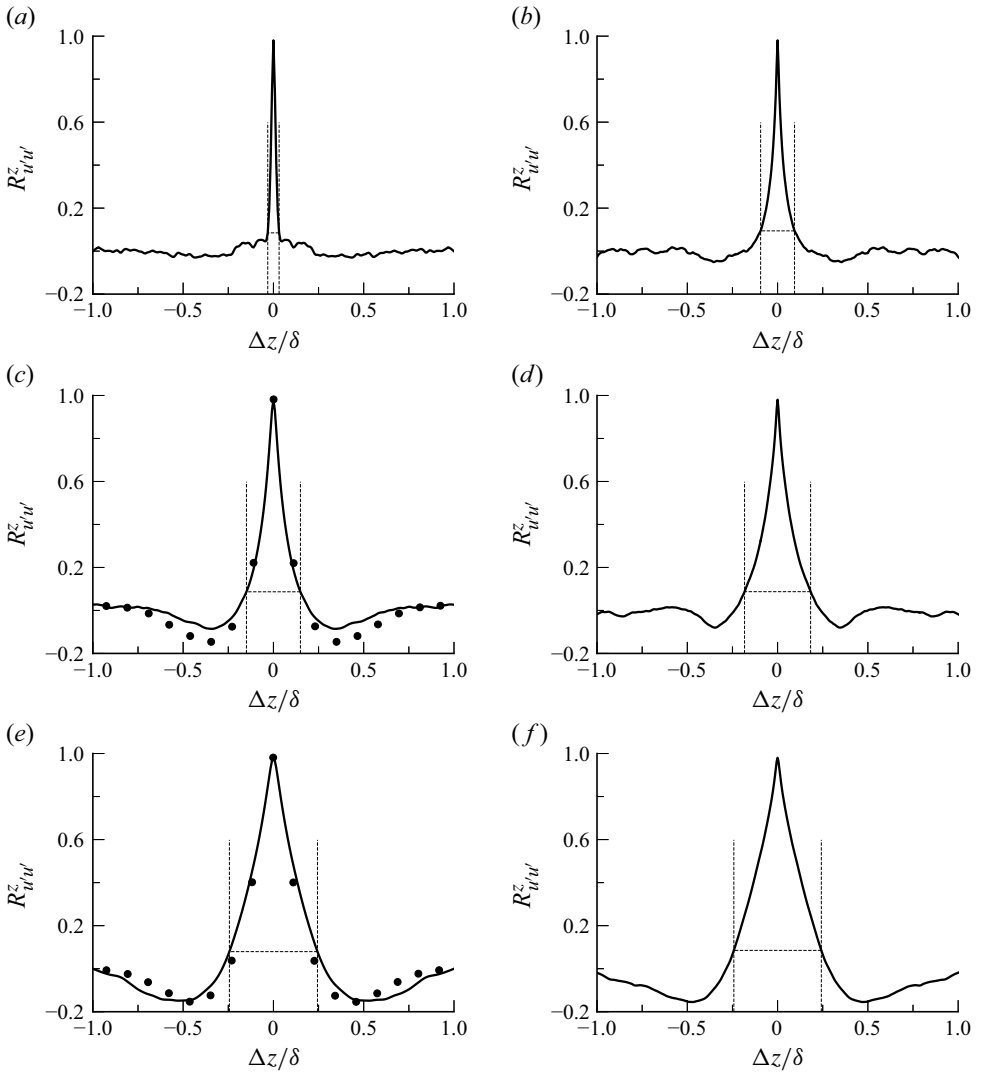

Figure 8. Spanwise two-point correlations of the streamwise velocity fluctuations, $R^z_{u'u'}$, at $x/\delta_{LE} = 62.5$ and various wall-normal locations. Left side: smooth wall, $Re_\tau = 1150$; right side: BR39 case $Re_\tau = 2900$; (*a*,*c*) at the centreline of viscous/roughness sublayer ($y/\delta_{smooth} = 0.005$, $y/\delta_{BR39} = 0.097$); (*b*,*d*) at the centreline of the logarithmic layer ($y/\delta_{smooth} = 0.083$, $y/\delta_{BR39} = 0.15$); (*e*,*f*) at the centreline of the outer layer ($y/\delta_{smooth} = 0.57$, $y/\delta_{BR39} = 0.59$); • experiments by Hutchins & Marusic (2007) at $Re_\tau = 1120$; dashed lines correspond to the correlation cutoff of $R^z_{u'u'} = 0.1$.

in the next section, different topographies result in different correlation lengths, $\mathscr{L}_x/\delta$, even for the same incoming *Re* boundary layer.

The spanwise extent (i.e. width) of the superstructures can be also computed from

$$R^z{}_{u'u'}(x,\, y,\, \Delta z) = \left\langle \sum_{n=1}^{N_z} \left[u'(x,\, y,\, z,\, t) u'(x,\, y,\, z + \Delta z,\, t)\right] / \sum_{n=1}^{N_z} \left[u'^2(x,\, y,\, z,\, t)\right] \right\rangle_t , \tag{3.2}$$

for the same streamwise and wall-normal locations and it is shown in figure 8 for both the smooth wall and the BR39 topography. Here, the whole spanwise extent of the

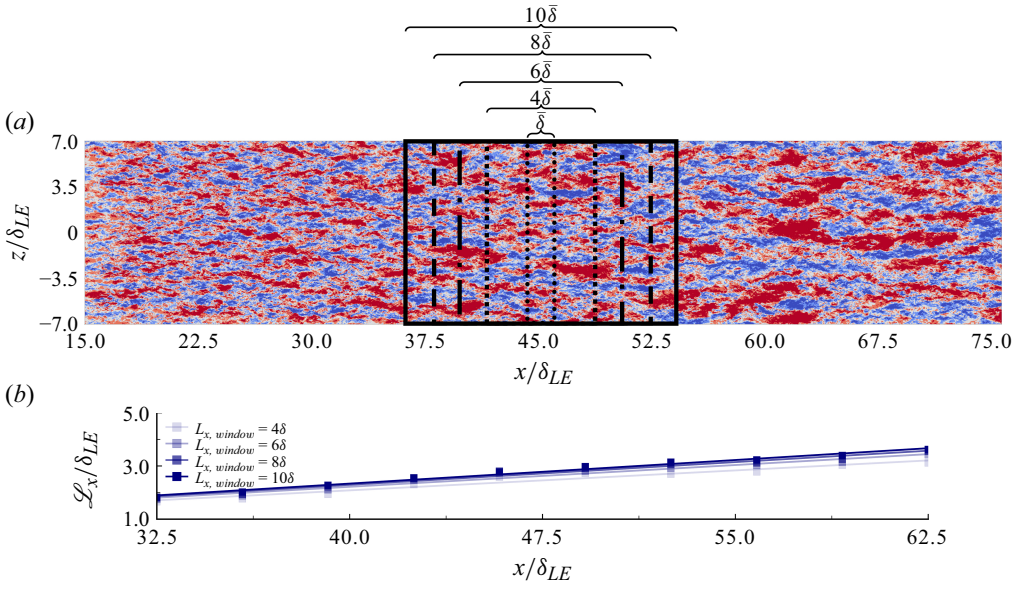

Figure 9. (*a*) Window size for the computation of $R^{x}_{u'u'}$; (*b*) evolution of the superstructure length, $\mathscr{L}_x$ (computed in the logarithmic layer for BR39 case), for different window sizes. Window lengths shown in legend. The reference boundary-layer thickness at the centre of the domain is equal to $\overline{\delta}_{BR39} \approx 1.8\delta_{LE}$.

computational box is used as a sampling window. From figure 8 we can infer that, contrary to the streamwise extent dependency on the wall-normal distance, in this case both the smooth wall and the BR39 topography exhibit larger widths as the wall-normal distance increases, reaching the boundary-layer edge. Figure 8(*c*,*e*) further validates the current findings regarding the smooth-wall superstructure shape when compared with the respective ones of Hutchins & Marusic (2007). It is noted that small differences in the latter in the strength of the anti-correlated regions could be attributed to the fact that the autocorrelation computed from the DNS data contains a much larger sample of superstructure entities in the spanwise direction compared with Hutchins & Marusic (2007). Figure 8 indicates shorter structures than the ones observed in figure 4. The latter is the result of the fact that the autocorrelation functions are averaged in time and thus they encapsulate the length of all flow structures not just of the largest/er ones that can be see in some instantaneous snapshots. Alternative approaches such as a curve fitting in the u' isosurfaces can easily bias the length estimates as they are entirely based on a given isosurface threshold, as well as on the order of the polynomial chosen to represent the curve, the selection of which is subjective. In addition, the u' isosurfaces often branch to other isosurfaces, thus making the selection of the superstructure direction ambiguous. On the other hand, the autocorrelation functions provide a length estimate based on a more mathematically rigorous, normalised coefficient.

Although, a single location measurement reveals a lot of information about the superstructure size, it does not provide any information about the growth of these structures along and across the boundary layer. Thus, their growth is captured herein by employing a windowing technique at various streamwise and wall-normal locations. Besides the streamwise and spanwise correlations we also compute the temporal correlation

$$R^{t}_{u'u'}(\underline{x}, \Delta t) = \sum_{n=1}^{N_t} \left[u'(\underline{x}, t)u'(\underline{x}, t + \Delta t)\right] / \sum_{n=1}^{N_t} \left[u'^2(\underline{x}, t)\right]. \tag{3.3}$$

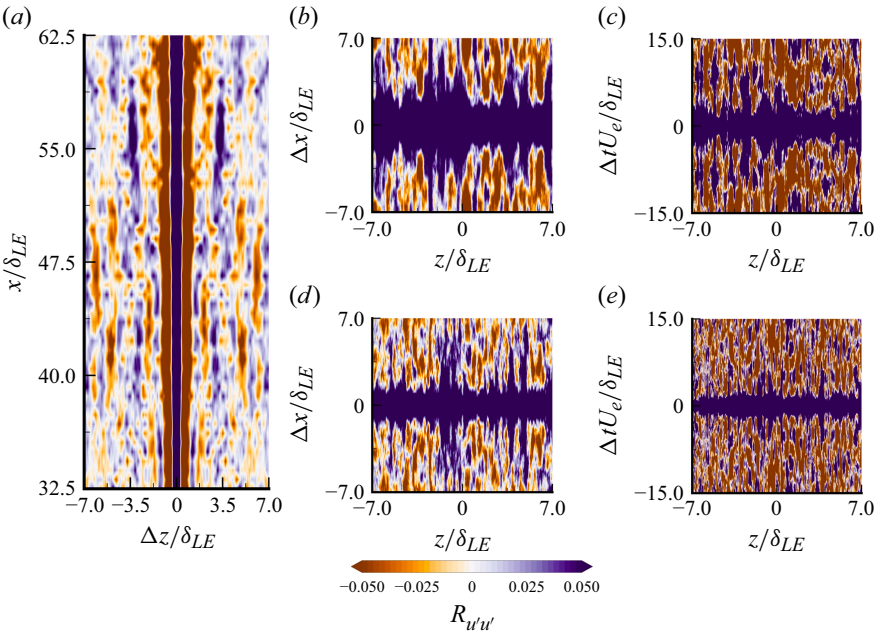

Figure 10. Contours of two-point correlations at the logarithmic layer with (*a*) spanwise lag, $R^z_{u'u'}$; (*b*), (*d*) streamwise lag, $R^x_{u'u'}$; (*c*), (*e*) temporal lag, $R^t_{u'u'}$; all in the case of the rough wall for the *BR*39 case; (*d*), (*e*) correspond to the streamwise location of $x/\delta_{LE} = 36$, while (*b*), (*c*) correspond to $x/\delta LE = 59$.

The size of the sampling window at different streamwise locations is well defined for the case of the spanwise, $R^z_{u'u'}$, and the temporal, $R^t_{u'u'}$, correlations and coincides with the size of the computational domain in the periodic spanwise direction and the length of the time-series velocity signal, respectively. For the case of streamwise correlations, $R^x_{u'u'}$, the sampling-window selection is not trivial because the correlation direction coincides with the direction in which the superstructures grow: if one selects the full streamwise extent of the domain, then the resulting streamwise correlations will be independent of the streamwise location, while if it is too narrow it will produce non-physical length scales. We conducted a sampling-window sensitivity analysis, where multiple windows of various lengths defined as an integer multiple of the local boundary-layer thickness, δ, are employed as shown in figure 9(*a*) relative to the flow scales in the case of the BR39 topography. The resulting length scales of the $R^x_{u'u'}$ correlations (all with same cutoff of 0.1) at various streamwise locations for the BR39 topography are plotted in figure 9(*b*). It can be seen that no significant effect is detected for window lengths greater than 6δ. In the case of the smooth wall the $\mathscr{L}_x/\delta_{LE}$ convergence is observed in windows of size 8δ and greater. Here, to ensure that even the largest instantaneous structures are captured, the window with extent equal to 10δ is chosen everywhere in the present work.

All two-point correlations were computed at ten streamwise locations separated by $3.4\delta_{LE}$, neglecting the leading and trailing parts of a roughness patch in order to eliminate any possible effects arising from the rough-to-smooth-wall transitions. Three wall-normal locations are considered as in figure 7. The streamwise evolution of the superstructure width can be seen in figure 10(*a*), where contours of $R^z_{u'u'}$ are shown at the logarithmic layer. The solid dark-blue region, which represents the spanwise correlation length or equivalently the width of the characteristic superstructure, is followed by a thin white region that corresponds to the correlation zero crossing. It is evident that this region

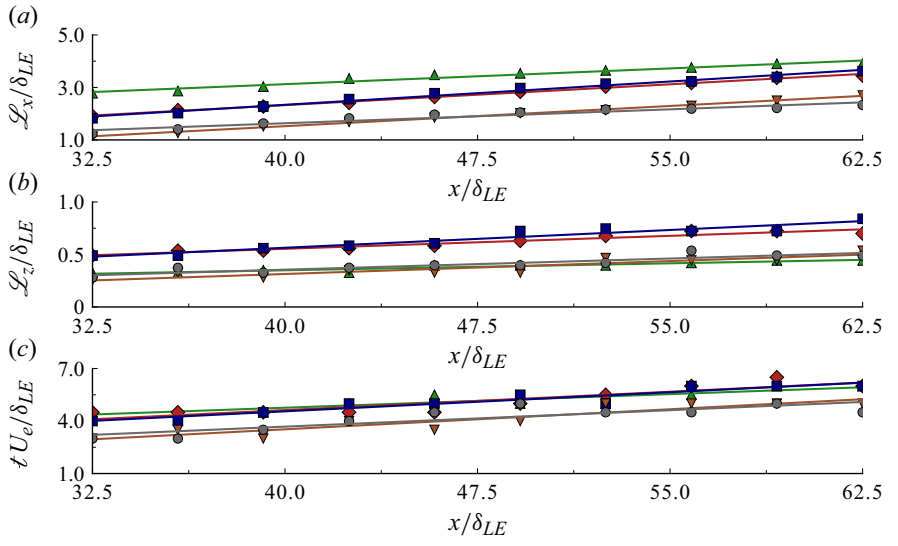

Figure 11. Streamwise evolution of: (*a*) length, $\mathscr{L}_x/\delta_{LE}$; (*b*) width, $\mathscr{L}_z/\delta_{LE}$; (*c*) time scale, $t\delta_{LE}/U_e$, of superstructures at the centreline of the logarithmic layer scaled by the smooth-wall leading-edge boundary-layer thickness. ▲ smooth wall; ◆ BS39; ■ BR39; ● MR39; ▼ TR39.

thickens as one moves downstream, indicating that the width of superstructures has an outer scaling growth which is in agreement with the qualitative observations in figure 4. Figure 10(*a*) indicates that the width growth of a characteristic superstructure is closely followed throughout the domain by one of different sign, shown in dark orange, representing the anti-correlated regions. Furthermore, the spanwise alternation of $R^z_{u'u'}$ implicitly confirms the spanwise alternation detected in the signs of the superstructures themselves. In addition, the spanwise variation of the superstructure length can be seen in figure 10(*b*,*d*), which is centred at two distinct streamwise locations at $x/\delta_{LE} = 36$ and $x/\delta_{LE} = 59$, respectively. The amplitude of the dark-blue region corresponding to the superstructure correlation length is significantly enhanced at the downstream location, providing further support for the outer scaling nature of superstructures. Finally, the superstructure characteristic time-scale variation with respect to the spanwise distance can be also seen in figure 10(*c*,*e*) for the same streamwise locations. Again, as in the case of the correlation lengths, the amplitude increases as the boundary layer grows, which suggests that larger-scale superstructures exhibit larger time scales. Very similar behaviour was also obtained for the rest of the topographical arrangements.

In order to more comprehensively capture the growth of superstructures within the boundary-layer, their spatio-temporal evolution is presented in figure 11 by performing a spanwise averaging over the full spanwise extent of the planar correlation maps shown in figure 10(*b*,*c*,*d*,*e*). Specifically, figure 11(*a*) suggests that the superstructure length grows faster over the rough-wall cases compared with the smooth wall, although no significant difference is observed between BS39 and BR39 indicating that the roughness distribution has minimal effect not just on the mean evolution of the boundary layer but also on its dynamics. Note that the latter observation does not necessarily imply that the roughness distribution has minimal impact on the flow in general, as it has been shown that flow phenomena such as the mean secondary motions maintain a strong dependency among others on the roughness distribution (see for example Barros & Christensen 2014; Kaminaris *et al.* 2023). The existence of increased superstructure lengths over

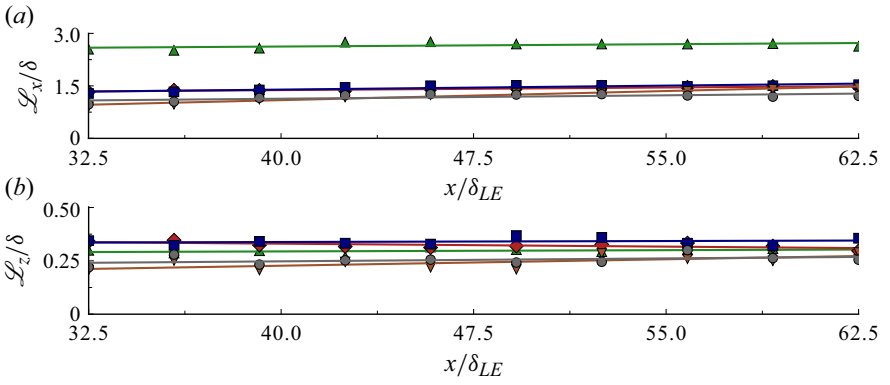

Figure 12. Streamwise evolution of: (*a*) length, $\mathscr{L}_x/\delta$; (*b*) width, $\mathscr{L}_z/\delta$ of superstructures at the centreline of the logarithmic layer scaled by the local boundary-layer thickness. ▲ smooth wall; ◆ BS39; ■ BR39; ● MR39; ▼ TR39.

the smooth-wall case compared with the rough-wall ones is probably a product of a breaking mechanism that takes place at the smooth-to-rough-wall transition, at which the coherence of incoming superstructures from the upstream smooth-wall portion of the computational domain is interrupted by the roughness elements. In the region downstream of the roughness leading edge the rough-wall superstructures reorganise themselves and eventually their streamwise coherence will surpass the respective one of the smooth-wall superstructures. The very good collapse of the correlation lengths from all the streamwise locations into a line strongly suggests that the outer scaling growth of superstructures follows a linear behaviour, at least up to $Re_\tau \leqslant 3000$. The same linear behaviour is also obtained for the widths of superstructures, which, similarly to the lengths, exhibit a higher growth rate in the cases of rough walls with minimal differences between BS39 and BR39 (barnacle-type only organisms). Similar arguments can be made for the time-scale evolution as well. More strikingly, the length scales when scaled by the local boundary-layer thickness (extracted at the middle of each sampling window) result in a constant ratio, $\mathscr{L}_x/\delta = c_1$ and $\mathscr{L}_z/\delta = c_2$, as shown in figure 12. This is found to be true for both the smooth-wall case and all the rough-wall cases, as well as across all the three major sublayers (here, only logarithmic-sublayer evolution is shown), and thus this non-dimensional length scale is believed to constitute a flow invariant. Strong support for the latter argument is implicitly provided by Hutchins & Marusic (2007), where two-point correlations computed in various Re_τ regimes collapsed into a single curve when scaled by the appropriate boundary-layer thickness. The latter is equivalent here to performing two-point correlations over different streamwise stations downstream in nominally the same boundary layer in which the Re_τ increases. Thus, scaling arguments could be made for flows of significantly higher Re. It should be stated that alternation of the correlation cutoff did not break the scaling at all, instead resulting in different c_1 and c_2 constants. Besides the correlation cutoff, the absolute values of the c_1 and c_2 constants are found to also depend on the underneath topography studied, while dependency on the characteristic Re of the flow remains to be investigated. Although figure 12 indicates overall constant $\mathscr{L}_x/\delta$ and $\mathscr{L}_z/\delta$ ratios for all the topographies, some cases show more deviation compared with the rest. The small discrepancies found in some of the case studies, i.e. TR39 and BS39, are believed to exist because of two main reasons. First, in the case of the streamwise length-scale ratios the small deviations are presumed to be the result of the fact that, although the streamwise autocorrelations are performed in windows, the centres of which

follow closely the sublayer growth rate, the autocorrelations *per se* are performed in the horizontal direction at each window. Thus, there might be a mismatch between the angle of the inclined superstructures and the horizontal direction of the correlations even within the window extent, which might also be to some degree case dependent. Second, there is an underlying assumption that the part of superstructures at each sublayer follows the sublayer growth, which might not be strictly true. Interestingly, the fact that the numerical experiments span a distance of $\approx 60\delta_{LE}$, at which the Re_τ is almost doubled (between the leading and trailing edges of the roughness), as well as that the surfaces under investigation differ significantly and still manage to sustain structures that grow with the boundary layer in a proportional fashion, provides strong support for the universal existence of such an invariants, $\mathscr{L}_x/\delta$ and $\mathscr{L}_z/\delta$. Finally, it is noted that the snapshots used to build the latter scale evolutions spanned a total time of $T \approx 34\overline{\delta}_{BR39}/U_e$ (where $\overline{\delta}_{BR39} \approx 1.8\delta_{LE}$), which in fact after performing spanwise averaging is equivalent to $T \approx 950\overline{\delta}_{BR39}/U_e$. Attention should be drawn to the fact that expanding in the spanwise direction does not necessarily yield independent flow samples, however, in the present case the spanwise autocorrelation functions of figure 11(*b*) act as a guide to inform us about the number of such independent samples and specifically they indicate that ≈ 28 (i.e. $L_{z,domain}/\mathscr{L}_{z,BR39} \approx 14/0.5 \approx 28$) distinct superstructures can be found across the spanwise extent of the boundary layer.

The analysis made so far provides an estimation of the superstructures size, as well as an insight into their streamwise evolution along the boundary layer. However, it does not provide any information regarding their 3-D silhouette. To address that, volumetric two-point correlations

$$R^{\underline{x}}_{u'u'}(x,\, y,\, \Delta\underline{x}) = \left\langle \sum_{n=1}^{N_{xyz}} \left[u'(\underline{x},\, t)u'(\underline{x}+\Delta\underline{x},\, t)\right] \Big/ \sum_{n=1}^{N_{xyz}} \left[u'^2(\underline{x},\, t)\right] \right\rangle_t, \tag{3.4}$$

are computed at three distinct regions of the boundary layer each of $10\delta \times 14\delta_{LE} \times \delta$ size in the streamwise, spanwise and wall-normal directions, respectively, centred at the centroid at $x/\delta_{LE} = 32$, $x/\delta_{LE} = 46$ and $x/\delta_{LE} = 59$ with respect to the streamwise coordinate and at $y/\delta = 0.5$ with respect to the wall normal. It is pointed out that, in the BR39 case, the volumetric region utilised in the two-point correlations is of $10\delta \times 14\delta_{LE} \times 0.9\delta$ size and thus centred at $y/\delta = 0.55$, because the wall-normal distance up to the nominal roughness crest is discarded. In this way a characteristic 3-D form of the superstructure evolution is obtained along the boundary layer and presented in figure 13(*a*,*b*). In the latter the positively correlated region depicting the characteristic superstructure of a given sign is shown in dark purple and the negatively correlated ones in dark orange; all scaled by the fixed smooth-wall incoming boundary-layer thickness δ_{LE} at the leading edge of the roughness. It is evident that as the superstructures move downstream they become longer and wider, as was also visually observed in figure 4. Furthermore, through the side view of figure 13(*c*,*d*) one can easily see that the superstructures are inclined with respect to the mean-flow direction, as well as that their shape changes as the boundary layer evolves, by stretching from slightly above the wall all the way to the boundary-layer edge. The latter is even more evident in the BR39 topography (figure 13*d*), where upstream superstructures that form an oval-like shape are converted into more elongated ones with pronounced 'tails' at the further downstream locations. Visual inspection of figure 5 reveals similar behaviour along the boundary layer, as expected. It should be noted that regarding the smooth-wall $R^{\underline{x}}_{u'u'}$, Sillero *et al.* (2014) and Kevin *et al.* (2019*b*) depicted structures of a very similar shape. However, they found that the correlations were not symmetric with respect to the streamwise lag, but rather enhanced at the negative-lag region.

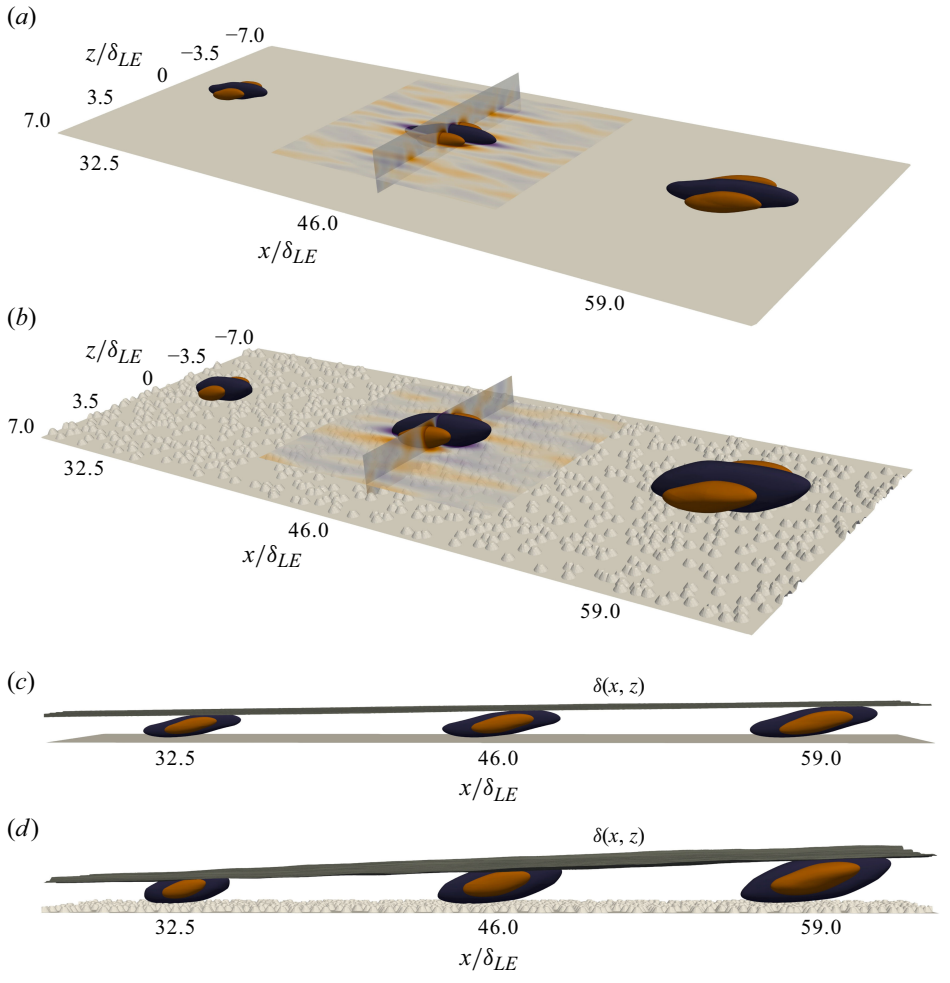

Figure 13. Isosurfaces of the time-averaged volumetric autocorrelations, $R^{\underline{x}}_{u'u'}(x, y, \Delta\underline{x})$, at three different streamwise stations in the case of (*a*), (*c*) the smooth wall and (*b*), (*d*) the BR39 case. (*a*), (*b*) Correspond to a 3-D view and (*c*), (*d*) to a streamwise/wall-parallel view of the same structures. Positive (dark-purple) isosurfaces are visualised with a threshold of 0.05 and negative (dark-orange) isosurfaces with −0.05.

The pronounced 'tails' in the isosurfaces of $R^{\underline{x}}_{u'u'}$ at the negative-lag regions are also well captured here, as mentioned above. However, it should be noted that, since volumetric correlations are used in the present work, the structures throughout the boundary layer are symmetric with respect to their local streamwise lag. On the other hand, when 2-D autocorrelations are performed at various wall-normal locations with respect to a fixed reference height (not shown here), i.e. $y/\delta \approx 0.5$, the resulting structures, although maintaining non-equal upstream and downstream correlation parts, were found to be more symmetric compared with the ones in Sillero *et al.* (2014) and Kevin *et al.* (2019*b*). This is probably due to the Re_τ differences between the present and Sillero *et al.* (2014) and Kevin *et al.* (2019*b*) studies. The friction Re ranges for the smooth wall and the BR39 topography shown in figure 13(*a–d*) are $850 \leqslant Re_\tau \leqslant 1100$ and $1900 \leqslant Re_\tau \leqslant 2800$, respectively. The smooth-wall boundary layer, despite clearly depicting a logarithmic layer, likely holds little separation between the near-wall and the outer-layer structures at $Re_\tau \approx 1000$ and thus

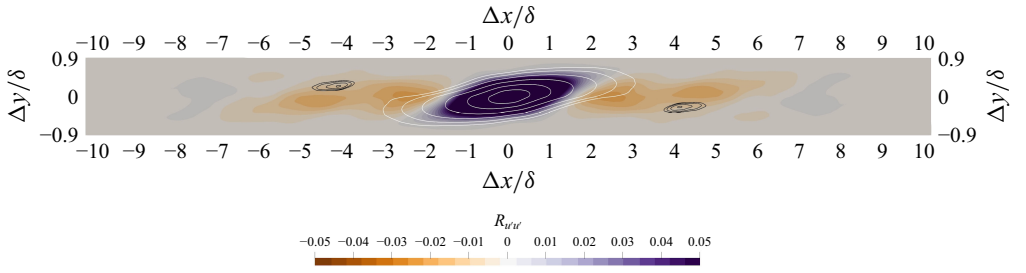

Figure 14. Side-view contours of the time-averaged volumetric autocorrelations, $R^{\mathscr{X}}_{u'u'}(x, y, \Delta x)$ for the BR39 topography extracted at $\Delta z = 0$, centred at $x/\delta_{LE} = 59$ and $y/\delta = 0.55$ and superposed by the respective smooth-wall isolines centred at $y/\delta = 0.5$ and at the same streamwise coordinate. Positive smooth-wall isolines (0.01, 0.02, 0.04, 0.08, 0.16, 0.32) are shown in white and negative isolines (−0.004, −0.0045, −0.005, −0.0055) in black; Note that, for the smooth-wall autocorrelation functions, $R^{\mathscr{X}}_{u'u'}$, the whole boundary-layer height is used, while for the BR39 topography only the boundary-layer part above the nominal roughness crest.

an increased inclination of $\overline{R}^{t}_{u'u'}$ towards the negative-lag region is expected at further downstream locations. The latter is in agreement with the arguments made in Hutchins & Marusic (2007) for smooth-wall boundary layers at a similar Re_τ, with which the current smooth-wall DNS data showed very good agreement, as was previously shown in figures 7 and 8(*a*,*c*,*e*). Finally, a 2-D comparison of the two-point correlations between the smooth wall and the BR39 topography centred at $x/\delta_{LE} = 59$ and $\Delta z = 0$ is shown figure 14 in terms of the local streamwise and wall-normal lag. It can be seen that the BR39 topography forms bulkier structures with steeper inclination angles compared with the smooth-wall ones, while in both cases anti-correlated regions are detected upstream and downstream of the main correlated region that are found to be stronger in the rough-wall case. Similar arguments where made in Kevin *et al.* (2019*b*) over a converging–diverging riblet surface. Volino *et al.* (2007) had also detected structures with stronger inclination angles under the presence of a rough wall. It is noted, however, that the smooth- and rough-wall comparison herein is made on the basis of the same streamwise coordinate given the presence of the same incoming boundary layer, δ_{LE}, and thus these differences may not hold when compared at the same Re_τ. Moreover, the positively correlated smooth-wall $R^{\mathscr{X}}_{u'u'}$ structure seems to be slightly longer, for a given isoline cutoff, as was also shown above from the 1-D correlations of figure 7. It should be noted, however, that the 1-D correlation functions do not directly correspond to the length scales captured by the volumetric correlation functions even in the case when the correlations are performed along a single direction, since in the latter a volume block is correlated and not just a 1-D signal, that is, structures located at different wall-normal locations.

4. Evidence of counter-rotating roll modes

An increased number of studies investigating the characteristics of superstructures in turbulent boundary layers have reported evidence of instantaneous counter-rotating vortices that flank the superstructures and exhibit streamwise coherence (see for example Marusic *et al.* 2021; Kevin *et al.* 2019*a*, 2019*b*). In this work we investigate the behaviour of such large-scale flow motions using modal analysis by means of POD. One could alternatively employ a low-pass filter (e.g. Gaussian) on the instantaneous velocity field, instead of performing a POD. The filter, however, would require a kernel size to be chosen

that even in the case that it would be associated with the autocorrelation length scales, it could in fact impose a specific length scale on the reconstructed flow field. On the other hand, when POD is employed the reconstructed flow field is based on the number of leading modes selected, which are freely elected to represent the most energetic structures, given enough of a time sample. We employ POD through the 'method of snapshots' which is ideal for cases where the number of spatial points is significantly increased compared with the number of instances (i.e. tall/skinny matrices), as in the current work. The method can be summarised in five main steps: (i) formation of the snapshot matrix, Y, for the velocity fluctuations as (n,m), where n stands for the total number of points of the two/three-dimensional field multiplied by the number of velocity components and m for the number of instances; (ii) computation of the temporal correlation matrix, $C_t = Y^T Y$, which will be of compact size (m,m); (iii) computation of the eigenvectors (or temporal coefficients), Ψ, and eigenvalues, λ, from $C_t \lambda = \lambda \Psi$; (iv) projection of the temporal eigenvectors onto the velocity field through the singular value decomposition definition to obtain the spatial eigenvectors, Φ; (v) construction of a reduced-order model (ROM) based on a lower number of modes, $\hat{u}' = \sum_{n=1}^{N} \alpha_n(t)\Phi_n(\underline{x})$. The ROM reconstruction for the whole 3-D field has been achieved by parallelising the POD algorithm using a classical domain decomposition along the streamwise direction by employing MPI library calls, which allowed for inter-core communication in order for the matrix C_t to be informed from the flow states along the whole extent of the boundary layer.

Here, we reconstruct the cross-plane velocity fluctuations by using only the first dominant mode, since the scope of the current study is not to create a ROM that could substitute the need for performing experiments/simulations, but rather to explore the underlying flow patterns in a lower-order flow field. The POD helps in identifying the latent large-energy-carrying structures, and it thus can be used as a 'filtering' operator to clean up the rather noisy instantaneous velocity field. Figure 15(a,b) shows the streamwise velocity fluctuations superposed by the magnitude-scaled cross-plane ones in vector format at a given instant and streamwise location in the case of the smooth wall and the BR39 topography, respectively. In figure 15(c,d) the ROM fields are shown for the same instant and streamwise location as in the figures above (figure 15a,b). One can thus readily detect that, in the ROM representations, well-shaped counter-rotating motions are formed, that are otherwise not visible in the original field, encharged with the cross-plane momentum redistribution. These counter-rotating motions are also found to flank the high- and low-speed superstructures; this behaviour holds true across the whole span of the boundary layer. It is also found that these vortical motions occur in fixed spanwise and wall-normal locations as time evolves, with the only major parameter being altered being their rotation sign, which changes to accommodate the superstructure passage through the cross-plane. The latter can be seen in figure 15(e,f) which shows the ROM of velocity fluctuations at a later instant. Hence, the observation of roll modes that flank the different sign superstructures is confirmed in both the smooth and rough walls. If one also factors in the excellent agreement observed in the outer-layer similarity (see figure 3d,e) it could be inferred that the way momentum organises itself in high Reynolds number wall-bounded flows might be independent of the roughness terrain underneath. The ROM in the rest of rough-wall cases, not shown here for brevity, follows the same behaviour, as well. It is also noted that the conjugate pair of counter-rotating vortices can be found at different wall-normal locations in spite of the fact they may flank the same superstructure. In fact, when the cross-plane vector fluctuations are not scaled by magnitude, one can easily observe that each roll mode exhibits a strength asymmetry compared with each conjugate pair and even across to its own reference core (not shown here). The latter is also in agreement

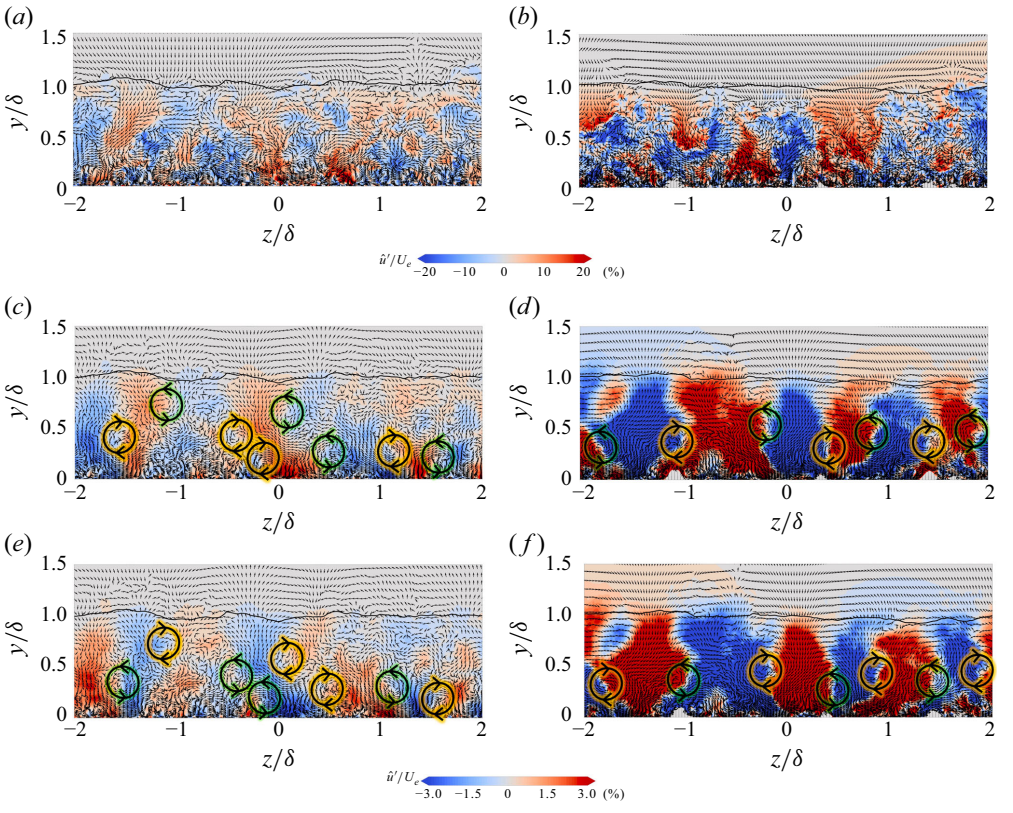

Figure 15. Cross-plane of streamwise velocity fluctuations scaled in local units at $x/\delta_{LE} = 65$. Top: original streamwise velocity fluctuations, u', for (*a*) the smooth wall ($Re_\tau = 1200$); (*b*) BR39 case ($Re_\tau = 3000$). Middle: ROM of streamwise velocity fluctuations, $\hat{u}'$, (only first most dominant mode) for (*c*) smooth wall; (*d*) BR39. Bottom: same as above at a later time instant when rotation sign changes.

with the observations made in Marusic *et al.* (2021) and Kevin *et al.* (2019*a*, 2019*b*). The instantaneous nature of the ROM field discussed here can be better understood through the visualisations provided in the accompanying movies. Furthermore, to enhance the validity of our observations a time sample and frequency sensitivity analysis is also performed for the BR39 topography that can be found in Appendix

In order to better understand the streamwise footprint of the counter rotating motions ROMs were constructed for the 3-D velocity fluctuation field of the whole extent of the boundary layer at a downscaled domain of a factor of four (by skipping one grid point in the streamwise and spanwise directions) to allow for a more computationally efficient analysis to be performed. A top view of the isosurfaces of the velocity fluctuations, $\hat{u}'$ superposed by the ROM $\hat{Q}$-criterion coloured by the streamwise fluctuating vorticity, $\hat{\omega}_x'$ can be seen in figure 16(*a*). It is evident that the roll modes detected in figure 15(*c–f*) preserve a significant streamwise coherence by closely following the superstructure evolution, as expected based on the 2-D superstructure representations of figure 15(*c–f*). It is noted that, besides the roll modes, the ROM superstructures themselves exhibit an increased streamwise coherence compared with the ones found in the original full-order flow field, as expected. Similar findings reported in Dong *et al.* (2023), who, through performing POD over a smooth-wall boundary, reconstructed a lower-order superstructure field with increased coherence and reduced noise. To better understand the interaction between the

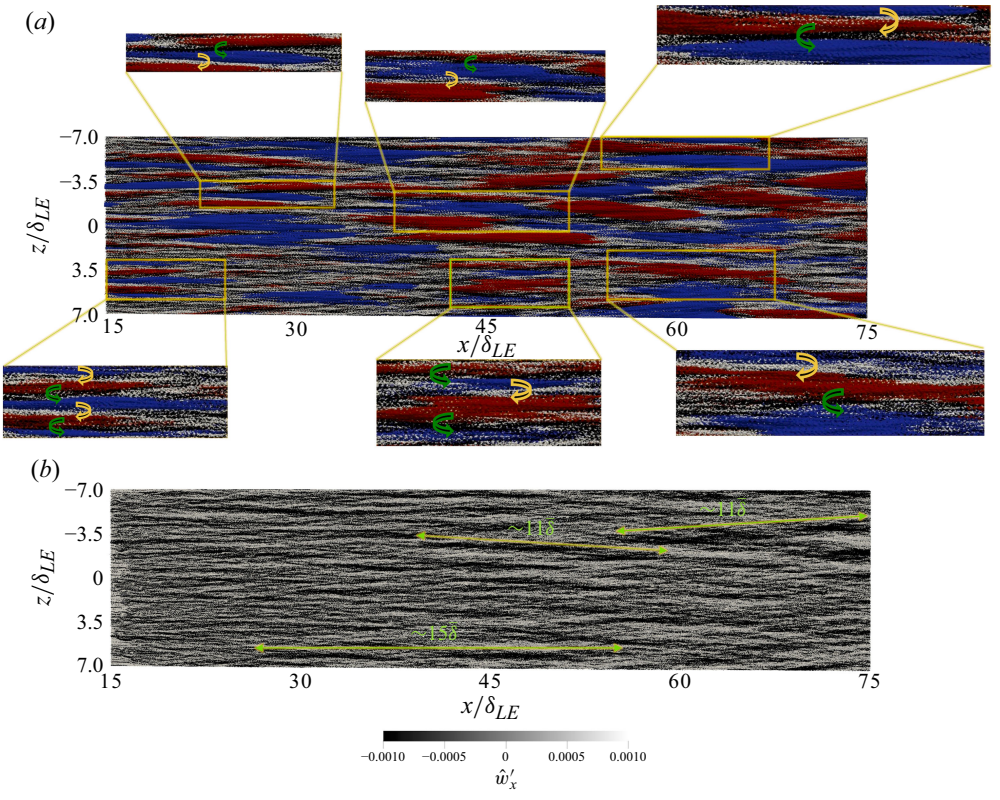

Figure 16. Reduced-order model of the flow accounting only for the highest energy mode; isosurfaces of high-speed superstructures at $\hat{u}'/U_e = 0.002$ shown in red and low-speed superstructures at $\hat{u}'/U_e = -0.002$ shown in blue; isosurfaces of $\hat{Q} = 1.7 \times 10^{-5}$ coloured by the streamwise vorticity fluctuations, $\hat{\omega}'_x$; all in the case of the rough wall with the random BR39 case.

superstructures and the counter-rotating vortices multiple magnified regions along the boundary layer are provided in figure 16(*a*). Specifically, it can be seen that clockwise vortices are formed between the low- to high-speed superstructures (by marching from the negative to the positive spanwise coordinates), transferring high momentum fluid from the upper portion of the boundary layer lower to the wall, as was also shown from the 2-D cross-sections of figure 15. Figure 16(*b*) isolates the isosurfaces of only the roll modes allowing for a cleaner depiction of their layout, which spans several boundary-layer thicknesses in the order of $10-15\overline{\delta}_{BR39}$. Finally, it is emphasised that these computations evolving whole boundary-layer volumetric DNS datasets are of high computational cost, with each POD run lasting for more than a week on two high-memory (3 TB) nodes processing over 1.7 TB of instantaneous data.

5. Conclusion

Direct numerical simulations were performed in smooth- and rough-wall spatially developing boundary layers up to $Re_\tau = 3150$ and 1-D two-point correlations were computed at three wall-normal and multiple streamwise locations in order to capture the spatio-temporal evolution of superstructures. It was found that the size of the superstructures grows faster in the rough-wall cases, when a fixed characteristic length scale is chosen as

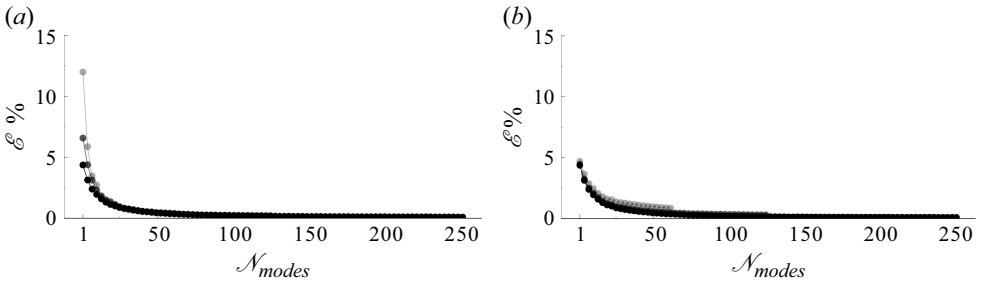

Figure 17. Energy distribution per mode for the case of (*a*) varying sample window at a fixed sampling rate $\Delta t = 0.135\overline{\delta}_{BR39}/U_e$ and (*b*) varying sampling rate at a fixed sample window of $T = 34\overline{\delta}_{BR39}/U_e$; darker circles correspond to increased sample window (left) or reduced sampling rate (right). Increments by a factor of two with $T_{max} = 34\overline{\delta}_{BR39}/U_e$ and $\Delta t_{min} = 0.135\overline{\delta}_{BR39}/U_e$; all in the case of the rough-wall BR39 arrangement by performing a 2-D POD. The reference boundary-layer thickness at the centre of the domain is equal to $\overline{\delta}_{BR39} \approx 1.8\delta_{LE}$.

the scaling factor, similar to the boundary-layer evolution in the mean field. Surprisingly, when the correlation lengths were scaled by the local boundary-layer thickness, the ratios $\mathscr{L}_x/\delta$ and $\mathscr{L}_z/\delta$ remained constant for the whole range of Re_τ along the boundary layer, indicating that such scaling might be a possible flow invariant. The latter argument is implicitly supported by the pioneering work of Hutchins & Marusic (2007) over smooth-wall boundary layers. The characteristic 3-D shape of the superstructures is captured throughout the boundary-layer evolution via volumetric correlations across the whole extent of the boundary layer. The reconstruction of a lower-order representation for the velocity fluctuating field via POD unveiled the underlying mechanisms of the cross-plane momentum redistribution that appear as counter-rotating roll modes which flank the superstructures and survive at locked spanwise and wall-normal locations, with their rotation sign being the only major parameter subject to time. The latter, in conjunction with the excellent agreement in the outer-layer similarity, strongly suggest that the way momentum organises itself in high Reynolds number wall-bounded flows might be independent of the roughness terrain underneath. In the future it would be interesting to explore the superstructure evolution under different scenarios such as in topographies with lower/higher blockage ratios, various smooth-to-rough-wall transition ratios, as well as in different *Re* regimes.

Supplementary movies. Supplementary movies are available at https://doi.org/10.1017/jfm.2025.10707.

Funding. Financial support from the US Office of Naval Research (ONR), under Grant No. N00014-19-1-2107 is gratefully acknowledged. All computational resources were provided by The George Washington University *Pegasus* high performance computing cluster.

Declaration of interests. The authors report no conflict of interest.

Appendix. The POD computation

In order to build a ROM that accurately captures the energy distribution per mode, a sensitivity study is performed and presented in figure 17(*a*,*b*) for two different case scenarios in the case of the BR39 arrangement; the first where the sampling rate is kept constant at $\Delta t = 0.135\overline{\delta}_{BR39}/U_e$ while the sample window is altered and the second where the sample window is kept constant at $T = 34\overline{\delta}_{BR39}/U_e$ while the sampling rate is altered. Thus, from figure 17(*a*) it can be concluded that the sample window has a significant effect on the energy distribution per mode, mainly for the first three modes. This is especially the case when just one quarter of the available time sample is used. On the

other hand, figure 17(*b*) suggests that the impact of the sampling rate has minimal effects on the per mode energy distribution when a large sample window is considered, similar to the findings of Wang *et al.* (2021). Therefore, this analysis underlines the importance of the sample window extent, which has to be large enough in order to contain multiple characteristic flow scales to accurately represent the velocity field.

References

Balaras, E. 2004 Modeling complex boundaries using an external force field on fixed Cartesian grids in large-eddy simulations. *Comput. Fluids* **33** (3), 375–404.

Barros, J.M. & Christensen, K.T. 2014 Observations of turbulent secondary flows in a rough-wall boundary layer. *J. Fluid Mech.* **748**, R1.

Chung, D., Hutchins, N., Schultz, M.P. & Flack, K.A. 2021 Predicting the drag of rough surfaces. *Annu. Rev. Fluid Mech.* **53** (1), 439–471.

Connelly, J.S., Schultz, M.P. & Flack, K.A.2006 Velocity-defect scaling for turbulent boundary layers with a range of relative roughness. *Exp. Fluids* **40**, 188–195.

Dennis, D.J.C. & Nickels, T.B. 2011 Experimental measurement of large-scale three-dimensional structures in a turbulent boundary layer. Part 1. Vortex packets. *J. Fluid Mech.* **673**, 180–217.

Deshpande, R., de, S., Charitha, M. & Marusic, I. 2023 Evidence that superstructures comprise self-similar coherent motions in high Reynolds number boundary layers. *J. Fluid Mech.* **969**, A10.

Dong, Z.X., Pan, C., Wang, J.J. & Yuan, X.X. 2023 Reduced-order representation of superstructures in a turbulent boundary layer. *Phys. Fluids* **35** (5), 055146.

Hutchins, N. & Marusic, I. 2007 Evidence of very long meandering features in the logarithmic region of turbulent boundary layers. *J. Fluid Mech.* **579**, 1–28.

Jiménez, J. 2004 Turbulent flows over rough walls. *Annu. Rev. Fluid Mech.* **36** (1), 173–196.

Kaminaris, I.K. & Balaras, E.2024 Direct numerical simulations of turbulent boundary layers developing over synthesised calcareous marine biofouling surfaces. *Ships Offshore Struct.* **0** (0), 1–12.

Kaminaris, I.K., Balaras, E., Schultz, M.P. & Volino, R.J. 2023 Secondary flows in turbulent boundary layers developing over truncated cone surfaces. *J. Fluid Mech.* **961**, A23.

Kevin, K., Monty, J. & Hutchins, N. 2019a The meandering behaviour of large-scale structures in turbulent boundary layers. *J. Fluid Mech.* **865**, R1.

Kevin, K., Monty, J. & Hutchins, N. 2019b Turbulent structures in a statistically three-dimensional boundary layer. *J. Fluid Mech.* **859**, 543–565.

Kim, K.C. & Adrian, R.J. 1999 Very large-scale motion in the outer layer. *Phys. Fluids* **11** (2), 417–422.

Lee, J., Kim, J.H. & Lee, J.H. 2016 Scale growth of structures in the turbulent boundary layer with a rod-roughened wall. *Phys. Fluids* **28** (1), 015104.

Lee, J., Sung, H.J. & Zaki, T.A. 2017 Signature of large-scale motions on turbulent/non-turbulent interface in boundary layers. *J. Fluid Mech.* **819**, 165–187.

Lee, J.H. & Sung, H.J. 2011 Very-large-scale motions in a turbulent boundary layer. *J. Fluid Mech.* **673**, 80–120.

Marusic, I., Chandran, D., Rouhi, A., Fu, M., Wine, D., Holloway, B., Chung, D. & Smits, A.J. 2021 An energy-efficient pathway to turbulent drag reduction. *Nat. Commun.* **12**, 5805.

Marusic, I., Mathis, R. & Hutchins, N. 2010 Predictive model for wall-bounded turbulent flow. *Science* **329** (5988), 193–196.

Schultz, M.P. 2007 Effects of coating roughness and biofouling on ship resistance and powering. *Biofouling* **23** (5), 331–341.

Sillero, J.A., Jiménez, J. & Moser, R.D. 2013 One-point statistics for turbulent wall-bounded flows at reynolds numbers up to $\delta^+ \approx 2000$. *Phys. Fluids* **25** (10), 105102.

Sillero, J.A., Jiménez, J. & Moser, R.D. 2014 Two-point statistics for turbulent boundary layers and channels at Reynolds numbers up to $\delta^+ \approx 2000$. *Phys. Fluids* **26** (10), 105109.

Smith, C.R. & Metzler, S.P. 1983 The characteristics of low-speed streaks in the near-wall region of a turbulent boundary layer. *J. Fluid Mech.* **129**, 27–54.

Squire, D.T., Morrill-Winter, C., Hutchins, N., Marusic, I., Schultz, M.P. & Klewicki, J.C. 2016*a* Smooth- *a*nd rough-wall boundary layer structure from high spatial range particle image velocimetry. *Phys. Rev. Fluids* **1**, 064402.

Squire, D.T., Morrill-Winter, C., Hutchins, N., Schultz, M.P., Klewicki, J.C. & Marusic, I. 2016*b* Comparison of turbulent boundary layers over smooth and rough surfaces up to high reynolds numbers. *J. Fluid Mech.* **795**, 210–240.

Townsend, A.A. 1976 The structure of turbulent shear flow.

VOLINO, R.J., SCHULTZ, M.P. & FLACK, K.A. 2007 Turbulence structure in rough-and smooth-wall boundary layers. *J. Fluid Mech.* **592**, 263–293.

WANG, Y., WANG, L., HU, R., KONG, L. & CHENG, J. 2021 Effects of sampling frequency on the proper orthogonal decomposition based reconstruction of a wind turbine wake. *IET Renew. Power Gen.* **15** (13), 2956–2970.

WANGSAWIJAYA, D.D. & HUTCHINS, N. 2022 Investigation of unsteady secondary flows and large-scale turbulence in heterogeneous turbulent boundary layers. *J. Fluid Mech.* **934**, A40.

WANGSAWIJAYA, D.D., BAIDYA, R., CHUNG, D., MARUSIC, I. & HUTCHINS, N. 2020 The effect of spanwise wavelength of surface heterogeneity on turbulent secondary flows. *J. Fluid Mech.* **894**, A7.

WOMACK, K.M., VOLINO, R.J., MENEVEAU, C. & SCHULTZ, M.P. 2022 Turbulent boundary layer flow over regularly and irregularly arranged truncated cone surfaces. *J. Fluid Mech.* **933**, A38.

WU, Y. & CHRISTENSEN, K.T. 2010 Spatial structure of a turbulent boundary layer with irregular surface roughness. *J. Fluid Mech.* **655**, 380–418.

ZAGAROLA, M.V. & SMITS, A.J. 1998 Mean-flow scaling of turbulent pipe flow. *J. Fluid Mech.* **373**, 33–79.

ÖRLÜ, R. & SCHLATTER, P. 2011 On the fluctuating wall-shear stress in zero pressure-gradient turbulent boundary layer flows. *Phys. Fluids* **23** (2), 021704.